Effect of dry density on the liquefaction behaviour of Quaternary silt

ZHANG Chong-lei[1,2,4] http://orcid.org/0000-0001-9718-6638; e-mail: zhangchonglei@imde.ac.cn

JIANG Guan-lu[2] http://orcid.org/0000-0002-7497-5623; e-mail: wgljiang@163.com

SU Li-jun[1,3,4]* http://orcid.org/0000-0001-9972-4698; ✉ e-mail: sulijun1976@163.com

Liu Wei-ming[1] http://orcid.org/0000-0002-8416-3530; e-mail: liuwm@imde.ac.cn

ZHOU Gong-dan[1,4] http://orcid.org/0000-0001-9014-2931; e-mail: gordon@imde.ac.cn

Corresponding author

1 Key Laboratory of Mountain Hazards and Earth Surface Processes, Institute of Mountain Hazards and Environment, Chinese Academy of Sciences, Chengdu 610041, China

2 Ministry of Education, Key Laboratory of High-speed Railway Engineering, School of Civil Engineering, Southwest Jiaotong University, Chengdu 610031, China.

3 CAS Center for Excellence in Tibetan Plateau Earth Sciences, Beijing 100101, China

4 University of Chinese Academy of Sciences, Beijing 100049, China

Citation: Zhang CL, Jiang GL, Su LJ, et al. (2018) Effect of dry density on the liquefaction behaviour of Quaternary silt. Journal of Mountain Science 15(7). https://doi.org/10.1007/s11629-018-4930-5

Abstract: Quaternary silt is widely distributed in China and easily liquefies during earthquakes. To identify the influence of the dry density on the liquefaction behaviour of Quaternary silt, 40 cyclic triaxial liquefaction tests were performed on loose silt (dry density ρ_d=1.460 g/cm³) and dense silt (ρ_d=1.586 g/cm³) under different cyclic stress ratios (*CSRs*) to obtain liquefaction assessment criteria, determine the liquefaction resistance, improve the excess pore water pressure (EPWP) growth model and clarify the relationship between the shear modulus and damping ratio. The results indicate that the initial liquefaction assessment criteria for the loose and dense silts are a double-amplitude axial strain of 5% and an EPWP ratio of 1. The increase in the anti-liquefaction ability for the dense silt is more significant under lower confining pressures. The *CSR* of loose silt falls well within the results of the sandy silt and Fraser River silt, and the dense silt exhibits a higher liquefaction resistance than the sand-silt mixture. The relationships between the *CSR* and loading cycles were obtained at a failure strain of 1%. The EPWP development in the dense and loose silts complies with the "fast-stable" and "fast-gentle-sharp" growth modes, respectively. The power function model can effectively describe the EPWP growth characteristics of the dense silt. Finally, based on the liquefaction behaviour of silt, a suggestion for reinforcing silt slopes or foundations is proposed.

Keywords: Liquefaction; Quaternary silt; Dry density; Earthquake magnitude; Liquefaction assessment; Cyclic stress ratio

Introduction

Statistics suggest that one-third of continental earthquakes with magnitudes M=7.0 or greater occur in mainland China. The magnitudes and
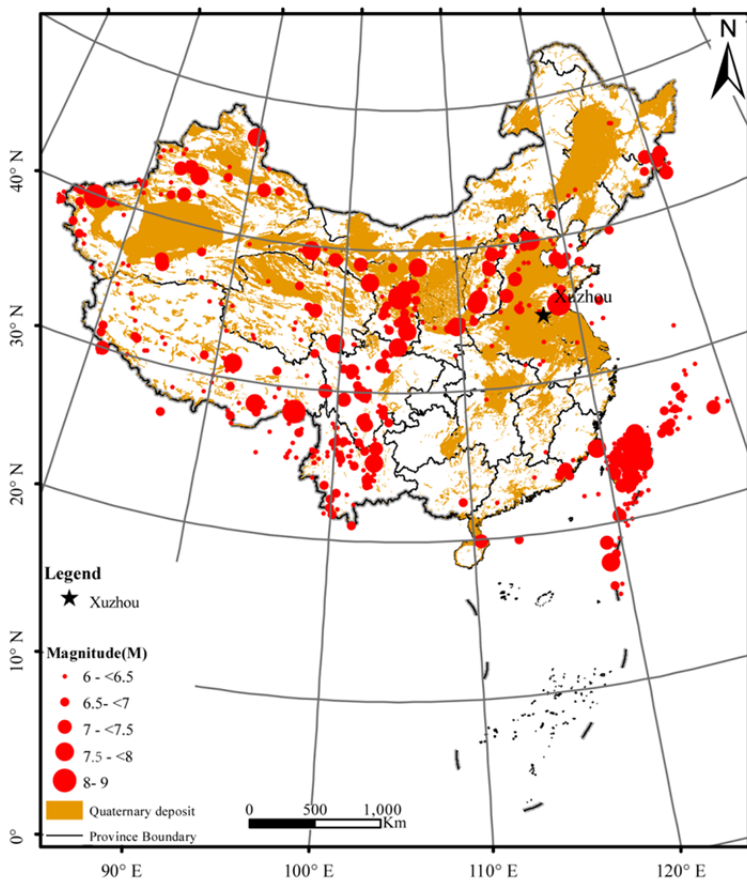
Figure 1 The distributions of earthquake magnitudes and Quaternary deposits in China and location of the sampling site (five-pointed star).

distribution of the earthquakes that have been identified throughout Chinese history were counted, as shown in Figure 1. In China, 41% of the territory and more than 50% of the cities are in areas with seismic intensity degree of at least VII. Since the 20th century, the death toll due to earthquakes in China has accounted for 54% of the total deaths due to all natural disasters, including floods, debris flows and landslides (Guo et al. 2016; Meng et al. 2016; Chen et al. 2018). Earthquake liquefaction is considered a typical natural hazard. Earthquake liquefaction can cause ground fissures, sandy boils or slope slip, thereby inducing serious geological disasters. Many of the intense earthquakes that have occurred worldwide resulted in catastrophic ground liquefaction (Monkul and Yamamuro 2011). Earthquake-induced sand liquefaction has led to massive infrastructure destruction, for example, as seen during the 1964 Niigata earthquake in Japan, the Alaska earthquake and 1971 San Fernando earthquake in the United States and the 1976 Tangshan earthquake in China (Guo et al. 2011).

The earthquake liquefaction due to the 1995 Kobe earthquake in Japan and the 1999 Kocaeli earthquake in Turkey led to road collapse, slope slip and the tilting of buildings (Gallagher and Mitchell 2002). In 2016, large-scale liquefaction occurred in the Tainan area during the Kaohsiung earthquake; the depth of liquefaction subsidence was 30-100 cm (Li and Yuan 2016). Soil liquefaction has become one of the main causes of earthquake damage to engineering structures. The United States and Japan have recently increased their soil liquefaction research efforts, and great progress has been made in the study of liquefaction; however, those studies have primarily focused on saturated clean sand (Monkul and Yamamuro 2011; Dashti et al. 2017; Shariatmadari et al. 2017; Tsaparli et al. 2017).

Silt with a low clay content can also be liquefied during an earthquake. Considerable large-scale liquefaction on silt foundations was identified in the following earthquakes: the Tangshan earthquake in 1976, the Chibaken-Tohooki earthquake in 1987, the Loma Prieta earthquake in 1989, the Hyogoken-Nanbu earthquake in 1995 and the Taichung earthquake in Taiwan in 1999 (Chen et al. 2013). Silt under earthquake action also becomes a potential liquefaction-prone soil (Qing et al. 2015; Huang et al. 2015; Beyzaei et al. 2018). Earthquake liquefaction of silt has become one of the most interesting phenomena in natural hazards research over the past decade (Sağlam and Bakır 2014; Khan et al. 2017). The behaviour of silt falls between that of fine sand and clay and has characteristics similar to those of sand and clay (Karim and Alam 2014; Taiba et al. 2016). However, significant differences also exist between silt and sand or clay. The distribution of Quaternary deposit types was primarily controlled by the geomorphological environment during deposition. The relative ubiety between the Quaternary deposit distribution and the earthquake magnitude M is given in Figure 1. Silt is the most common sediment in the small topographic undulations of plains and central

basins. As shown in Figure 1, silt is widely distributed in the Tangshan area, Qiantang River area, Haihe River basin, middle and lower reaches of the Yellow River, riverbanks areas and coastal areas; furthermore, silt is commonly deposited in areas with historically high earthquake magnitudes (Chen et al. 2013). Consequently, the problem of silt liquefaction in earthquake prone areas is imminent (Adhikari et al. 2018).

The previous literature on sand liquefaction mainly focused on the following aspects: (i) effects of the confining pressure (Yamamuro and Lade 1997; Thevanayagam 1998); (ii) effects of the fine particle contents (Georgiannou 2006; Rahman et al. 2014; Monkul et al. 2016); (iii) liquefaction mechanisms (Okamura and Soga 2011; Alibolandi and Ziaie 2015; Thevanayagam et al. 2016); (iv) sample preparation methods (Yamamuro et al. 2008; Mahmoudi et al. 2016); and (v) effects of cyclic shear strain (Sivathayalan and Ha 2011; Chiaro et al. 2012). Due to the unique particle composition of silt (combination of sand, silt particles and clay), the liquefaction process of silt is clearly different from that of sandy soil (Hyde et al. 2006; Hsu et al. 2017). The latest research on silt liquefaction has mainly focused on liquefaction resistance (Okamura and Noguchi 2009; El Takch et al. 2016; Chegenizadeh et al. 2018) and the effect of the fines content (Belkhatir et al. 2011; Stamatopoulos et al. 2015; Porcino and Diano 2017) on the liquefaction mechanisms, among other characteristics. Although the liquefaction characteristics of granular materials are affected by their dry densities and the applied cyclic shear stresses, how those factors affect the liquefaction resistance and excess pore water pressure (EPWP) of silt has not yet been sufficiently studied (Wang et al. 2016; Chegenizadeh et al. 2018). Therefore, the influence of the dry density on the entire process of silt liquefaction should be explored. Forty cyclic triaxial liquefaction tests were performed on Quaternary saturated silts to obtain the liquefaction resistance, dynamic strength and response characteristics of the EPWP to propose an EPWP growth model of loose silt (dry density ρ_d=1.460 g/cm³) and dense silt (ρ_d=1.586 g/cm³) and to analyse the evolution of the shear modulus and damping ratio. This investigation on the liquefaction process of Quaternary silt can aid in forecasting seismic liquefaction disasters and mastering liquefaction prevention methods.

1 Sample preparation

Samples were taken from the Quaternary (Q_4^{al}) alluvial silt in Xuzhou, Jiangsu Province, China. The location of the sampling point is shown in Figure 1. The ground motion peak acceleration of this area is 0.1 g. The thickness of the silt is 6.5-8.5 m. The silt has yellowish and brownish particles and is loose, moderately dense, and mostly saturated. The groundwater is mainly pore phreatic water and extends to a depth of 0-0.6 m. Standard penetration tests (SPTs) and shear-wave velocity tests (SWVTs) were mainly carried out in the initial stage of field sample preparations. During the sampling process, preliminary liquefaction assessments were carried out. The SPTs and SWVTs were used for preliminary liquefaction assessments of the sampling points.

The blow counts N_t of the in situ criterion for the SPT of the silt sampling site are shown in Figure 2. A total of 12 groups of liquefaction assessments in four boreholes were compared with the GB50111-2006 specification. Eqs. (1)-(5) were adopted to obtain the critical penetration blow counts N_{cr} of the silt layer liquefaction (GB50111-2006). Silt liquefaction is defined as $N_{cr} > N_t$ (Price et al. 2016). An in situ liquefaction assessment was conducted on the silt layer at a depth of 0-8 m, and the silt in the sampling point was defined as liquefied silt.
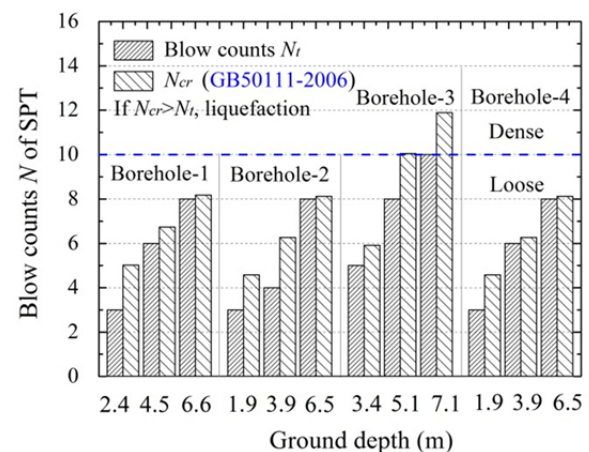

Figure 2 Preliminary liquefaction assessments of the silt layer from SPTs and the definition lines of the degree of density.

$$N_{cr}=N_o\alpha_1\alpha_2\alpha_3\alpha_4 \tag{1}$$

$$\alpha_1=1-0.065(d_w-2) \tag{2}$$

$$\alpha_2=0.52+0.175d_s-0.005d_s{}^2 \tag{3}$$

$$\alpha_3=1-0.05(d_u-2) \tag{4}$$

$$\alpha_4=1-0.17\sqrt{P_c} \tag{5}$$

where N_{cr} is the critical penetration blow count of liquefaction; N_o is the criterion blow count, when the ground motion peak acceleration is 0.1 g, and $N_o=6$; α_1 is the correction coefficient of the groundwater depth d_w (m), and $d_w=0$ m; α_2 is the SPT correction coefficient of the sample point depth d_s (m); α_3 is the correction coefficient of the overlying non-liquefied layer depth d_u (m); and α_4
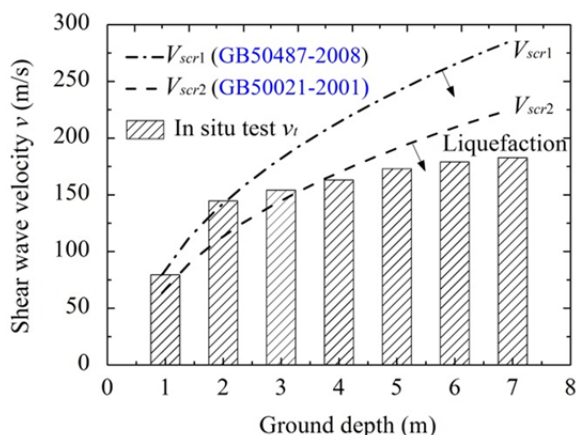

Figure 3 Preliminary liquefaction assessments of the silt layer from in situ shear-wave velocity tests and the critical shear-wave velocities (V_{scr1} and V_{scr2}) calculated by specifications GB50487-2008 and GB50021-2001.
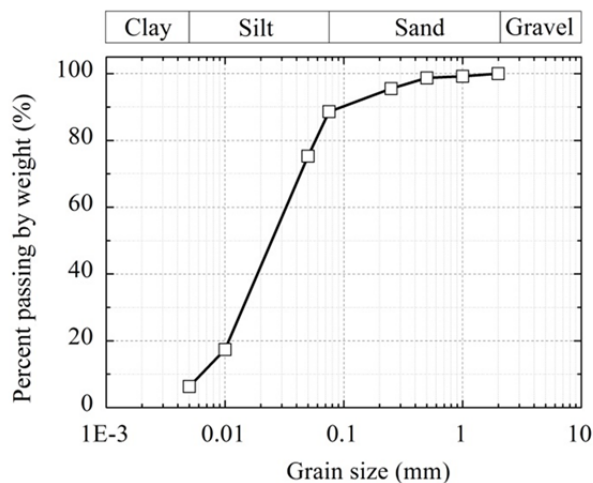

Figure 4 Particle size distributions of the silt sample used in this study.

is the correction coefficient of the clay content P_c, and $P_c=6.3\%$. If $I_p\leq7$, $\alpha_4=0.6$, and if $7<I_p\leq10$, $\alpha_4=0.45$.

Figure 3 shows the results of the shear-wave velocities v_t in the situ silt layer. The GB50487-2008 and GB50021-2001 specifications were adopted to calculate the critical shear-wave velocities V_{scr1} and V_{scr2} of the liquefied silt layer. When the shear-wave velocity v_t of the silt is less than the upper bound of the shear-wave velocity calculated by Eq.(6) obtained from GB50487-2008, it can be classified as liquefied silt.

$$V_{scr1} = 291\sqrt{K_H \cdot d_s \cdot r_d} \tag{6}$$

where V_{scr1} is the critical value of the shear-wave velocity (m/s); K_H is the peak acceleration coefficient of the earthquake motion, $K_H=a_{max}/g$; d_s is the soil depth; and r_d is the depth correction coefficient, $r_d=1.0-0.01d_s$.

Furthermore, the liquefaction assessment of Eq. (7) obtained from GB50021-2001 is

$$V_{scr2} = V_{s0}(d_s - 0.0133d_s{}^2)^{0.5} \tag{7}$$

where V_{so} is a reference value for determining the shear-wave velocity of liquefaction. When the seismic intensity degree is IX, the V_{so} of silt is 90 m/s.

As shown in Figure 3, $V_{scr1}>v_t$ or $V_{scr2}>v_t$, and the SWVT result is consistent with the SPT result; thus, the sampling point of the silt layer is also considered to be a liquefied silt by the evaluation of the critical shear-wave velocities.

1.1 Physical and mechanical properties

The sampled silt has a natural weight of 18.2-20.1 kN/m³, specific gravity of 2.70-2.72, and natural void ratio of 0.6-1.0. The liquid limit, plastic limit and plasticity index I_P of the silt are 25.7-29.5, 17.5-23.1, and 6.4-8.2, respectively, as shown in Table 1. Figure 4 shows the grading curve of the silt soil, where the slit particle content constitutes most of the soil, which has smaller sand and clay contents. The particle content with a grain size greater than 0.075 mm is 11.4%, and it is less than 50% of the total mass of the sample. This sample is defined as silt according to GB50007-2002 because $I_P \leq10$ and the particle content of the grain sizes greater than 0.075 mm does not exceed 50% of the total weight. According to SL299-1999

Table 1 Basic physical and mechanical properties of the silt samples.

Natural water content (%)	Natural unit weight (kN/m³)	Specific gravity G_s	Liquid limit (%)	Plastic limit (%)	Plastic index (%)
21.5-34.3	18.2-20.1	2.70-2.72	25.7-29.5	17.5-23.1	6.4-8.2
Natural void ratio e_0	Compressibility coefficient $a_{0.1-0.2}$ (MPa)	Compressibility modulus $E_{s0.1-0.2}$ (MPa)	Percent of particles (%)		
			0.25-0.075 (mm)	0.075-0.005 (mm)	<0.005 (mm)
0.6-1.0	0.2-0.4	4.7-11.5	11.4	82.3	6.3

and ASTM D2487-98, this sample is defined as a low liquid limit silt (ML) because more than 85% of the particles pass through a No. 200 sieve (0.075 mm), I_P<7.0, and this sample plots below the A-line in the plasticity chart.

1.2 Preparation of the static triaxial tests

The effect of the dry density of Quaternary silt on the static shear strength was tested. To compare the difference between the static drained strength and the dynamic undrained strength, the static shearing behaviour under monotonic loading was first investigated through consolidated drained triaxial tests by using the method described in SL237-1999. All of the triaxial tests were performed on a dynamic triaxial testing system (DYNTTS) manufactured by Geotechnical Digital Systems Instruments Ltd. at the Institute of Mountain Hazards and Environment, the Chinese Academy of Sciences. The technical parameters for these tests are listed in Table 2.

Silt samples with dry densities of ρ_d=1.460 g/cm³ (denoted as loose silt, e_0≥0.85, and N_t<10) and ρ_d=1.586 g/cm³ (denoted as dense silt, e_0≤0.75, and N_t>15) were selected. For the ρ_d=1.586 g/cm³ silt, the initial void ratio was e_0=0.70, the saturated unit weight was 20 kN/m³, and the silt was considered to be in a dense state. The sample preparation method followed Wang et al. (2011). The sample dimensions were 50 mm×100 mm (diameter×height, ϕ×h). The samples underwent evacuation and back-pressure saturation, and the

Table 2 Main technical parameters of the dynamic triaxial testing system used in the tests

Force accuracy (%)	Axial load (kN)	Data acquisition (points/s)
<0.1	2.0	100
Displacement accuracy (%)	Axial maximum displacement (mm)	Max. frequency (Hz)
<0.07	90	5

saturation criterion used was Skempton EPWP B ≥95%. The consolidated confining pressures σ_3 were 50, 100 and 150 kPa. The consolidation stability criterion was a volume change rate of ΔV<0.1 mL/hour. The shear rate was 0.05 mm/min to create full drainage (Monkul and Yamamuro 2011; Hyde et al. 2006). During the tests, if the axial strain ε_a reached 15% or the deviator stress reached the peak value, shearing was immediately stopped.

1.3 Preparation of the cyclic triaxial liquefaction tests

Table 3 shows the experimental programmes of the 40 cyclic triaxial liquefaction tests. Under the conditions of dry density (ρ_d=1.460 g/cm³ or 1.586 g/cm³) and effective confining pressure (σ_3=50, 100, or 150 kPa), 40 cyclic triaxial liquefaction tests under different cyclic stress ratios (*CSRs*) (Table 3) were performed. The sample size and consolidation method of the tests were consistent with those of the static triaxial tests in section 1.2. Polito et al. (2013) stated that the liquefaction energy dissipation of saturated sand was independent of the loading waveform. Therefore, a constant axial sinusoidal loading at a frequency of 0.1 Hz was applied in the tests. The initial axial loading force at the cyclic loading centre was defined as 0.002 kN, and the stiffness coefficient was defined as 0.2 kN/mm.

Due to the short duration of the earthquake, the soil remained undrained during the earthquake. An axial dynamic stress σ_d (σ_d=F_d/S, where F_d is the amplitude of the axial dynamic load, and S is the cross-sectional area of the sample) was applied to the samples. The consolidation stress and undrained condition persisted, and the dynamic shear stress on the 45° plane of the sample was τ_d=σ_d/2, where τ_d was used to simulate the shear stress on the horizontal surface of the silt layer in the field. Table 3 shows the amplitude of the axial load F_d applied to the samples under different dry

densities. The data sampling frequency during the cyclic loading process was 100 Hz. The liquefaction criterion of saturated silt is defined as either $u/\sigma_3=1$ or when the double-amplitude axial strain $2\varepsilon_{amax}$ reaches 5% (SL237-1999), and multiple cycles were applied after reaching the initial liquefaction assessment criteria. The EPWP u and axial strain ε_a were measured under different CSRs ($CSR=\tau_d/\sigma_3=\sigma_d/2\sigma_3=F_d/2S\sigma_3$) to obtain the number of loading cycles to liquefaction failure N_f.

2   Test Results and Discussion

2.1 Shear strength under monotonic loading

Figure 5 shows the relationship between the deviator stress q ($q=\sigma_1-\sigma_3$) and axial strain ε_a for saturated silts with $\rho_d=1.460$ g/cm³ (loose silt, $e_0=0.86$) and $\rho_d=1.586$ g/cm³ (dense silt, $e_0=0.70$). The peak deviator stress for the $\rho_d=1.586$ g/cm³ silt is clearly greater than that of the $\rho_d=1.460$ g/cm³ silt. A greater sample consolidation confining pressure and density can improve the silt shear strength. Due to the larger granular pores of the loose silt ($\rho_d=1.460$ g/cm³), the pore walls collapse, the pores shrink under shear stress, and the deviator stress increases with the axial strain (solid line). The characteristics of shear-shrinkage without clear peaks and the stress-strain relationship of the loose silt follow a strain hardening pattern.

After the deviator stress q of the saturated dense silt ($\rho_d=1.586$ g/cm³) reaches the peak value, it decreases (dotted line), showing the characteristics of dilatancy. The stress-strain relationship curve of the dense silt follows a strain softening pattern. Due to the smaller granular pores of the dense silt, the particles are limited to slipping along the contact points and surfaces under shear stress. When the shear stress increases to overcome the interlocking effect between the silt particles, the deviator stress q reaches its peak. The particles are then rearranged, and the sample reaches a steady state.

The peak value of the deviatoric stress was used as the failure point. The K_f strength line was plotted by connecting the zenith points of the failure stress circles. The subscript f denotes the state of failure. The K_f shear strength lines are shown in Figure 6. Table 4 shows the shear strength parameters of the saturated silt. When the dry density ρ_d increases from 1.460 g/cm³ to 1.586 g/cm³, the effective cohesion c' and effective internal friction angle φ' increase by approximately 6.5 kPa and 1.0°, respectively. Increasing the compaction of the silt effectively improves its

Table 3 Experimental programmes of 40 cyclic triaxial liquefaction tests of the silt sample used in this study.

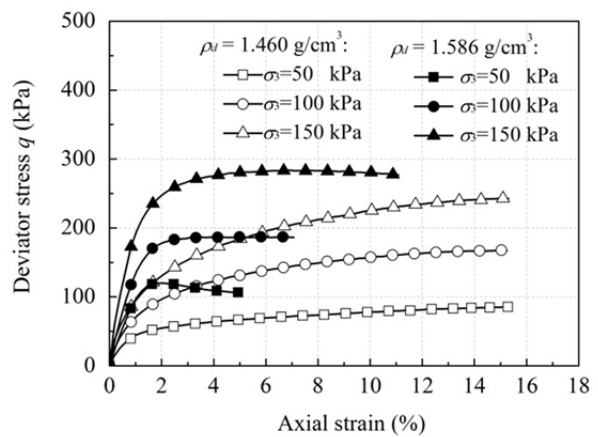| ρ_d (g/cm³)	Confining pressure σ_3 (kPa)	Applied axial dynamic load F_d (kN)
1.460	50	0.01, 0.012, 0.014, 0.016, 0.02, 0.024
	100	0.04, 0.045, 0.05, 0.055, 0.06
	150	0.05, 0.06, 0.065, 0.07, 0.08, 0.10, 0.12
1.586	50	0.08, 0.09, 0.10, 0.11, 0.12, 0.14, 0.16
	100	0.14, 0.15, 0.16, 0.18, 0.20
	150	0.16, 0.17, 0.18, 0.19, 0.20, 0.22, 0.25

Figure 5 Deviator stress q versus axial strain ε_a of the silt samples silts with $\rho_d=1.460$ g/cm³ (loose silt, $e_0=0.86$) and $\rho_d=1.586$ g/cm³ (dense silt, $e_0=0.70$).
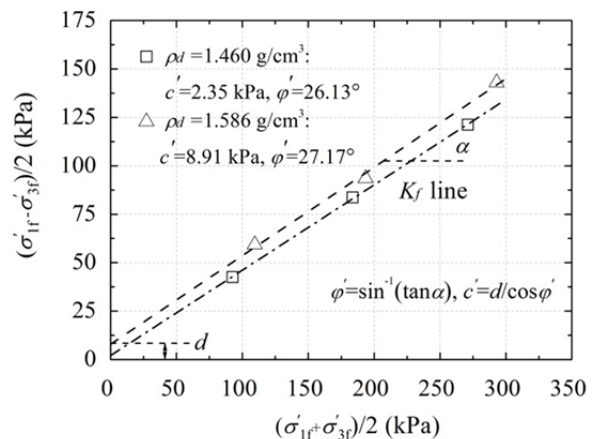

Figure 6 K_f shear strength lines and shear strength parameters of the loose silt and the dense silt.

Table 4 Peak shear strength q_{max}, cohesion c' and internal friction angle φ' of the silt samples under two dry densities.

ρ_d (g/cm³)	σ_3 (kPa)	ε_a (%)	q_{max} (kPa)	c' (kPa)	φ' (°)	$q_{max}/(2\sigma_3)$
	50	15	85.026			0.85
1.460	100	15	167.365	2.35	26.13	0.84
	150	15	242.334			0.81
	50	1.88	118.712			1.19
1.586	100	5.62	187.124	8.91	27.17	0.94
	150	7.24	285.962			0.95

Note: the yield strength ratio $q_{max}/2\sigma_3$ is defined as the peak shear strength q_{max} normalized by the confining pressure $2\sigma_3$.

cohesion. The yield strength ratio $q_{max}/2\sigma_3$ was applied to determine the soil failure (Olson and Stark 2003). The ranges of the yield strength ratio $q_{max}/2\sigma_3$ of the two types of silt (ρ_d=1.460 g/cm³ and 1.586 g/cm³) are 0.81-0.85 and 0.94-1.19, respectively. Increasing the dry density significantly increases the yield strength of the silt. The obtained shear strength and yield strength ratio allow a stability analysis of the silt slope to be conducted.

2.2 Liquefaction behaviour under cyclic loading

2.2.1 Liquefaction assessment criterion

Figures 7a-7f show the time-history curves of the dynamic response parameters under σ_3=50, 100 and 150 kPa and include (i) the axial stress σ_a (ii), the EPWP u, and iii) the axial strain ε_a under different confining pressures. For the silt with ρ_d=1.460 g/cm³ (Figures 7a, 7c, 7e), in the initial stage of cyclic loading, the EPWP u and the dynamic axial strain ε_a increase slowly. With an increase in the loading cycles, ε_a increases considerably, and the double-amplitude axial strain of $2\varepsilon_{max}$ reaches the initial liquefaction failure criterion ($2\varepsilon_{max} \geq 5\%$). Simultaneously, after the accumulation of the EPWP, u begins to increase rapidly with a decrease in σ_a but remains lower than the confining pressure σ_3 when liquefaction failure occurs. This process is very similar to that of sand liquefaction (Monkul and Yamamuro 2011). During the initial stage of cyclic loading, the u value
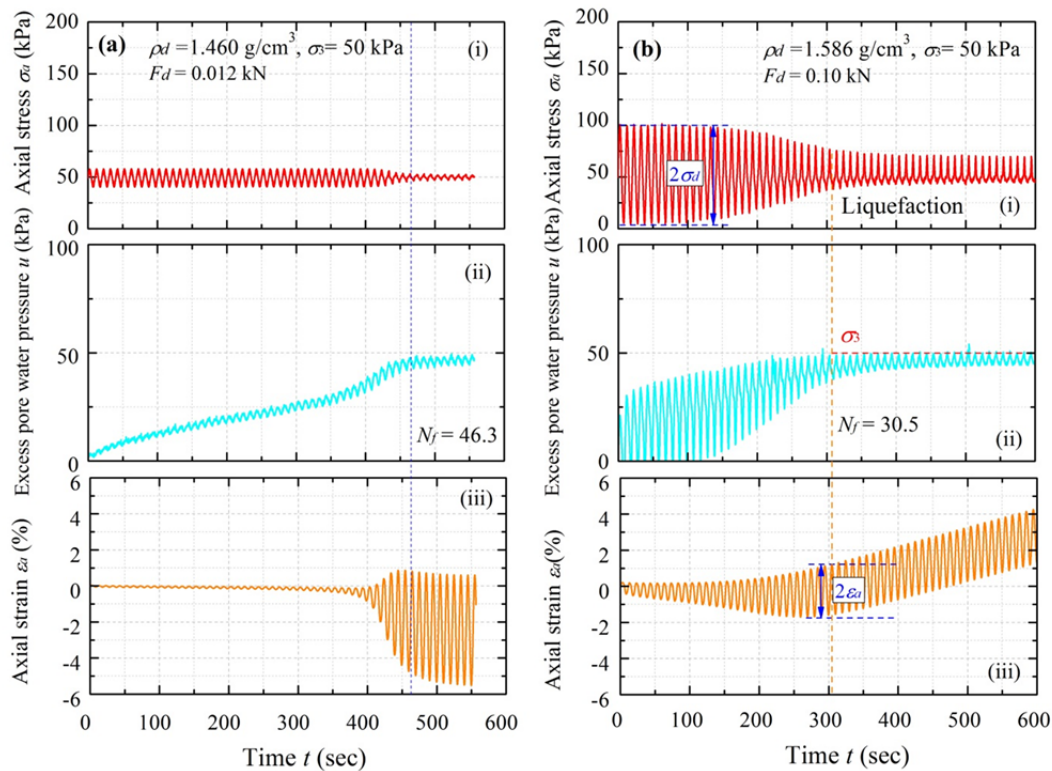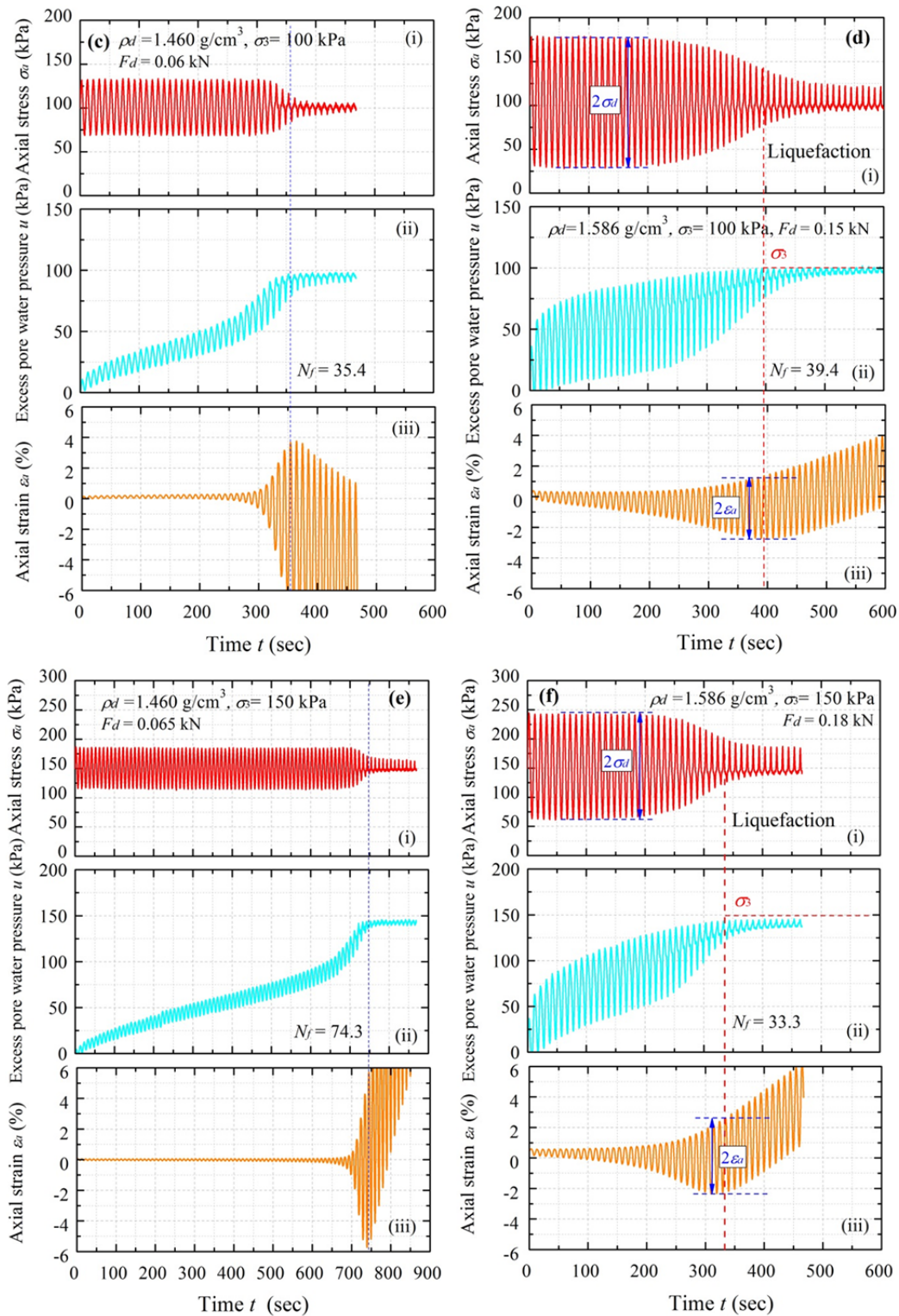

Figure 7 Time-history curves of the (i) axial stress σ_a, (ii) excess pore water pressure (EPWP) u, and (iii) axial strain ε_a under different confining pressures: a) ρ_d=1.460 g/cm³, σ_3=50 kPa, and F_d=0.012 kN; b) ρ_d=1.586 g/cm³, σ_3=50 kPa, and F_d=0.065 kN; c) ρ_d=1.460 g/cm³, σ_3=100 kPa, and F_d=0.06 kN; d) ρ_d=1.586 g/cm³, σ_3=100 kPa, and F_d=0.15 kN; e) ρ_d=1.460 g/cm³, σ_3=150 kPa, and F_d=0.065 kN; and f) ρ_d=1.586 g/cm³, σ_3=150 kPa, and F_d=0.18 kN. (-To be continued-)

(Continued-)

(-Continued-) **Figure 7** Time-history curves of the (i) axial stress σ_a, (ii) excess pore water pressure (EPWP) u, and (iii) axial strain ε_a under different confining pressures: a) ρ_d=1.460 g/cm³, σ_3=50 kPa, and F_d=0.012 kN; b) ρ_d=1.586 g/cm³, σ_3=50 kPa, and F_d=0.065 kN; c) ρ_d=1.460 g/cm³, σ_3=100 kPa, and F_d=0.06 kN; d) ρ_d=1.586 g/cm³, σ_3=100 kPa, and F_d=0.15 kN; e) ρ_d=1.460 g/cm³, σ_3=150 kPa, and F_d=0.065 kN; and f) ρ_d=1.586 g/cm³, σ_3=150 kPa, and F_d=0.18 kN.

of the ρ_d=1.586 g/cm³ silt undergoes a rapid increase (Figures 7b, 7d, 7f). After a few loading cycles, u reaches the consolidation confining pressure (u/σ_3=1), the viscosity between the particles resists the shear stress, and liquefaction occurs in the silt layer. During this process, ε_a sustains stable growth until liquefaction failure, but $2\varepsilon_{max}$<5% when liquefaction occurs. For the loose saturated silt, considering the influence of the response lag of u, a double-amplitude axial strain of $2\varepsilon_{max}$=5% could accurately reflect the initial liquefaction assessment criteria. However, for the dense silt with a low permeability, an EPWP ratio of 1 is a more suitable liquefaction criterion.

The incremental build-ups of the EPWP u with an increase in the number of loading cycles N_f for the dense silt and the loose silt are distinctly different. The EPWP of the loose silt and incohesive sand (Monkul and Yamamuro 2011) rises slowly in the initial stage of cyclic loading but suddenly increases when close to liquefaction. The EPWP development of dense silt at the initial stage of cyclic loading is not as smooth as that in the later stage of cyclic loading but rather fluctuates. The sharp increase in the EPWP of the dense silt at the initial stage of cyclic loading is because the permeability coefficient of dense silt is smaller than those of loose silt and fine sand, and the pore water pressure in the soil is not easily dissipated and transferred, and thus, a large volumetric strain is produced, and the structure of soil is rapidly destroyed. In contrast, due to the presence of fine particles and the small amount of clay particles, the silt has a certain structural strength and cohesive strength, which hinders and restricts the increase in the EPWP, resulting in the slow growth in the pore pressure in the later stage of cyclic loading until it tends to stability.

2.2.2 Liquefaction strength of silt

To compare the liquefaction strength of silt under different dry densities (ρ_d=1.460 g/cm³ and 1.586 g/cm³), u/σ_3=1 is defined as the unified liquefaction criterion. Figure 8 shows the relationship between the dynamic shear stress τ_d and the number of loading cycles required to cause liquefaction N_f, namely, the liquefaction strength curve. The dry density has a significant influence on the liquefaction strength, and the liquefaction resistance of silt is improved with greater densities.
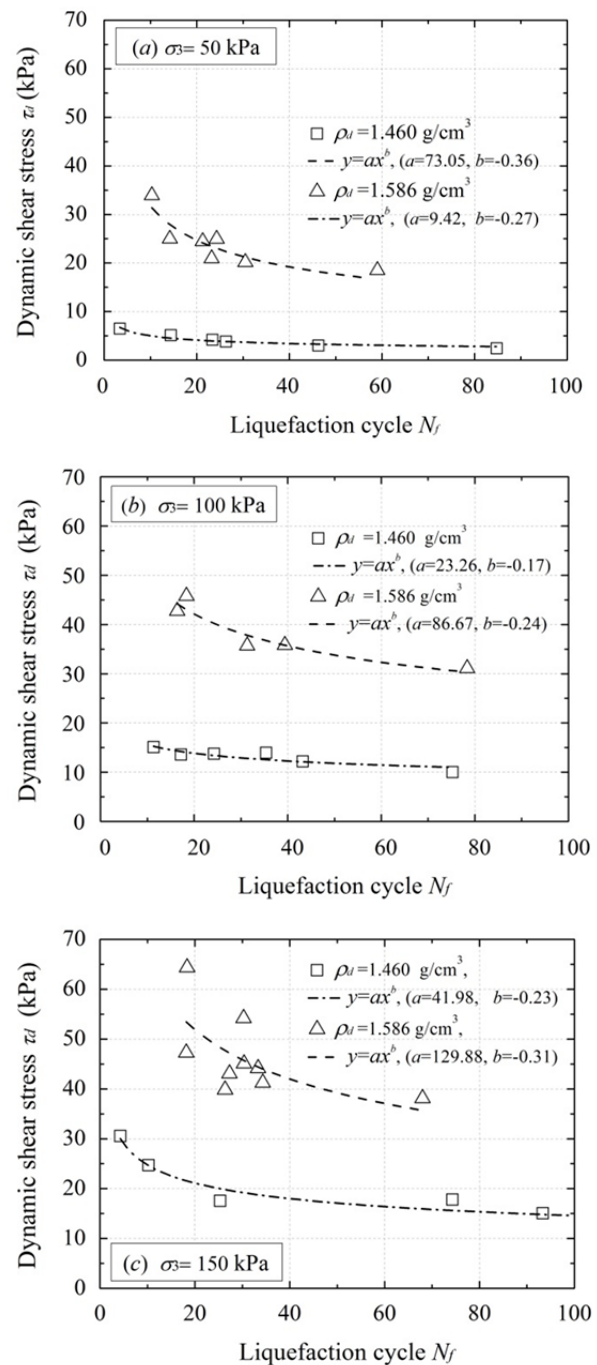

Figure 8 The relationships between the cyclic shear stress and the number of loading cycles required to cause initial liquefaction N_f in the silt samples under different confining pressures.

The dynamic shear stress τ_d required for liquefaction decreases as the loading cycles for liquefaction failure N_f increase. The dynamic shear stress τ_d increases with an increase in the confining pressure σ_3. The accumulated energy dissipation of liquefied silt increases with the confining pressure,

improving the liquefaction resistance. A positive linear relationship is observed between the liquefaction energy dissipation of sand and confining pressure (Baziar and Sharafi 2011). Compared with the dynamic shear stress τ_d of the ρ_d=1.460 g/cm³ silt, that of the ρ_d=1.586 g/cm³ silt increases by factors of approximately 5, 3 and 2 under the confining pressures of σ_3=50 kPa, 100 kPa, and 150 kPa, respectively. The smaller the confining pressure, the more significant the increase in dry density is to increase the liquefaction resistance.

Figure 9 shows the relationships between the *CSR* and the number of loading cycles required to cause liquefaction N_f during the initial liquefaction failure. The *CSR* of silt decreases with an increase in the number of liquefaction cycles N_f. The *CSR* of the loose silt increases with an increase in the confining pressure, while the *CSR* of the dense silt decreases with an increase in the confining pressure. The increase in the dry density at a lower confining pressure greatly influences the increase in the *CSR*. When the confining pressures are 50 kPa, 100 kPa and 150 kPa, the *CSR* of dense silt increases by approximately 5 times, 3 times and 2 times, respectively, compared with that of the loose silt. The increase in the anti-liquefaction ability of the dense silt is more significant under lower confining pressures. In other words, the effect of an increase in the dry density on the anti-liquefaction of the shallow silt is better than that of the deep silt.

Idriss and Boulanger (2008) indicate that the relationship between the *CSR* and N_f can be generally presented as

$$CSR=\alpha(N_f)^\beta \qquad (8)$$

in which α and β are the fitting parameters that are summarized in Figure 9. The parameter α is the *CSR* of the soil for one loading cycle and varies with factors that affect the liquefaction resistance (e.g., density and gradation) (El Takch et al. 2016). The exponent β is typically approximately 0.26-0.31 for dense silt and close to 0.21-0.28 for loose silt in this study. The average β for the dense silt of this study is close to that (β=0.34) obtained for clean sands (Boulanger and Idriss 2004). The average β for the loose silt of this study is close to that (β=0.19) obtained for fine-grained tailings materials (Wijewickreme et al. 2005).

The experimental data of the loose silt (ρ_d=1.460 g/cm³) and the dense silt (ρ_d=1.586 g/cm³) were compared with the results suggested for sandy silt and Fraser River silt obtained by El Takch et al (2016) and for Ticino sand-silt mixtures obtained by Porcino and Diano (2017), as shown in Figure 9. As can be seen in Figure 9, the *CSR* of loose silt falls well within the results of the sandy silt and Fraser River silt obtained by El Takch et al (2016) at σ_3=100 kPa, which may be due to the similar dry densities. The differences in particle arrangements and particle gradations cannot be fully reflected in the loose silt. The *CSR*s of dense silt are obviously higher than the results for the Ticino sand-silt mixtures obtained by Porcino and Diano (2017) at σ_3=100 kPa. The particle size of silt in the dense silty soil is smaller than that of fine sand particles, and its specific surface area is relatively large, which has some characteristics of a cluster structure. In addition, the physicochemical
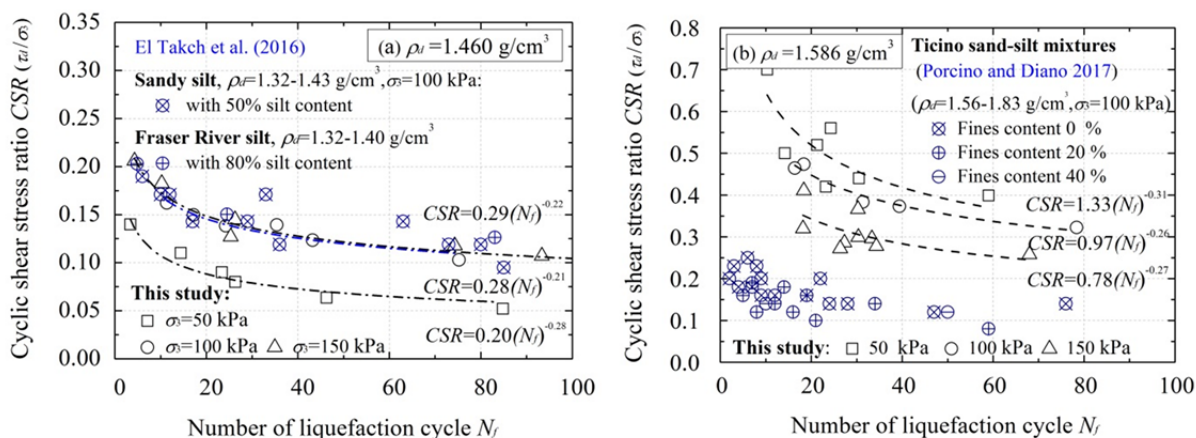

Figure 9 The relationships between the *CSR* and the number of loading cycles required to cause liquefaction N_f in silt samples under different confining pressures: (a) ρ_d=1.460 g/cm³; (b) ρ_d=1.586 g/cm³.

action of clay particles and the bonding effect of water in pores are also included in silt. The abovementioned influencing factors cause the dense silt to have a higher structural strength than the sand-silt mixtures and to often exhibit a higher liquefaction resistance than the sand-silt mixtures.

Earthquakes have random amplitudes and reciprocating loads, and seismic liquefaction assessment often equates the seismic load to the sinusoidal load under a specified number of loading cycles. The corresponding loading cycles of liquefaction failure N_f were obtained according to different earthquake magnitudes M. Then, the dynamic shear stress τ_d corresponding to N_f was obtained from Figure 9 to establish the quantitative relationship between the earthquake magnitude M and liquefaction-resistant CSR, as shown in Figure 10.

The dry density is an important factor on the earthquake-induced liquefaction of silt, namely, the liquefaction resistance increases with a greater dry density. For example, for an earthquake magnitude M=8.0, the CSR of the dense silt is nearly 107.5% higher than that of the loose silt at a confining pressure of 150 kPa. The liquefaction resistances for the loose silt and the dense silt decrease with an increasing earthquake magnitude M. For earthquake magnitudes greater than 7.0, the attenuation rate of the liquefaction resistance increases with the earthquake magnitude. In the seismic design of engineering structures, the density of the silt can be increased to enhance the liquefaction resistance of silt foundations or slopes.

2.2.3 Dynamic strength of silt

Dynamic strength refers to the dynamic stress required to cause a specified failure strain ε_{af} under cyclic loading; therefore, the dynamic strength is related to the liquefaction criteria and the loading cycles N/N_f. The axial strain amplitude of the specimen reaches 1% as the failure criterion during the tests. Figure 11 shows the dynamic strength curve (CSR-N/N_f relationship) when the failure strain reaches ε_{af}=1%, where τ_d/σ_3 is the CSR required for liquefaction and N/N_f is the normalized number of loading cycles. The confining pressure of consolidation has a weak effect on the relationship between the liquefaction-resistant CSR and loading cycles N/N_f at the failure strain of ε_{af}=1%. The dynamic strength of the silt
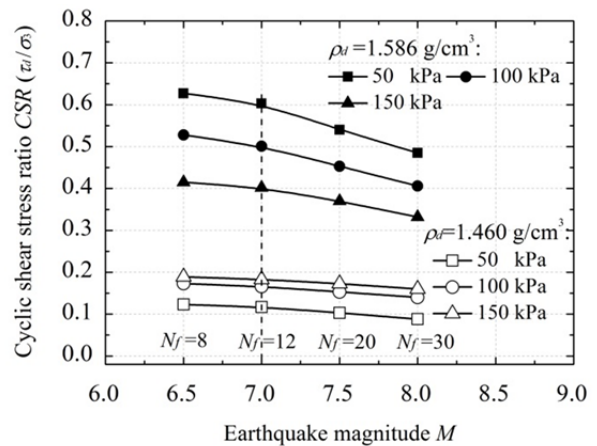
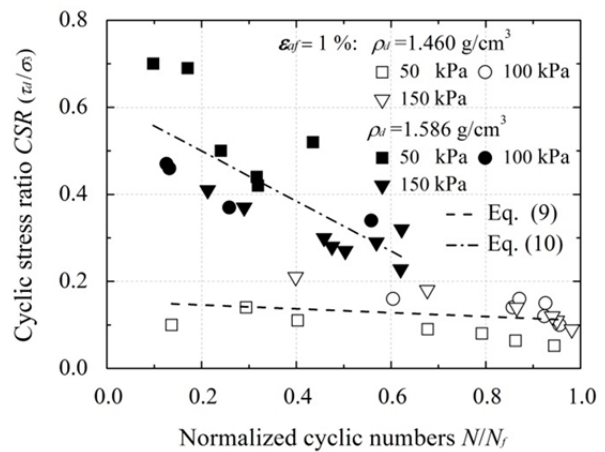**Figure 10** Relationships between the earthquake magnitudes M and liquefaction-resistant CSR.

Figure 11 Cyclic stress ratio (CSR) τ_d/σ_3 versus the normalized number of cycles N/N_f for an axial failure strain of ε_{af}=1% under different confining pressures.

increases with the dry density. The CSR-N/N_f curves were linearly fitted to obtain the dynamic strengths in Eq. (9) and Eq. (10) of saturated silts with ρ_d=1.460 g/cm³ and ρ_d=1.586 g/cm³, respectively, at a failure strain of 1%:

$$CSR=0.155-0.044N/N_f \quad (\rho_d=1.460 \text{ g/cm}^3), \quad (9)$$

$$CSR=0.615-0.575N/N_f \quad (\rho_d=1.586 \text{ g/cm}^3). \quad (10)$$

2.2.4 Excess pore water pressure (EPWP)

The increase in the EPWP in liquefiable soils under dynamic loading is the major cause of liquefaction during earthquakes. Seed et al. (1975) developed an empirical model for predicting the residual EPWP ratio (u/σ_3), which is defined as the ratio of the residual excess pore pressure u to the initial effective stress σ_3 acting on the soil. Figure

12 shows the typical EPWP u versus the dynamic axial strain relationship due to cyclic loading at a confining pressure of σ_3=50 kPa. As shown in Figure 12, the relationship between the EPWP and axial strain ε_a of loose silt (ρ_d=1.460 g/cm³) shows a mushroom-shaped distribution, whereas the dense silt (ρ_d=1.586 g/cm³) presents a sickle-shaped distribution. At the beginning of cyclic loading, the strain of loose silt is small (ε_a<0.5%), and u continues to rise, which is in the stage of cumulative shear. When u exceeds 35 kPa, the increase in the axial strain amplitude is much higher than that in the EPWP. In the unloading process of the dynamic stress, the negative axial strain amplitude increases and the value of u decreases, whereas the value of u increases rapidly with an increase in ε_a in the loading stage.

The EPWP of dense silt (ρ_d=1.586 g/cm³) is very sensitive to an increase in the axial strain amplitude. In the initial stage of cyclic loading, the value of u increases rapidly to 30 kPa, and the interval between the positive and negative values of EPWP is very large. Afterwards, in the process of increasing the strain amplitude, the growth rate of the EPWP slows down with the continuous development of the axial strain, and the EPWP gradually becomes stable in the later stage of loading. The intervals between positive and negative values of the EPWP amplitude decrease.

To explore the trend of the EPWP of silt at different dry densities, Figure 13 shows the growth curves of the EPWP ratio (u/σ_3) with the number of loading cycles (N/N_f). As the number of loading cycles N/N_f increases, u/σ_3 increases. The variations in the dynamic stress weakly influence the u/σ_3-N/N_f curve under a consistent confining
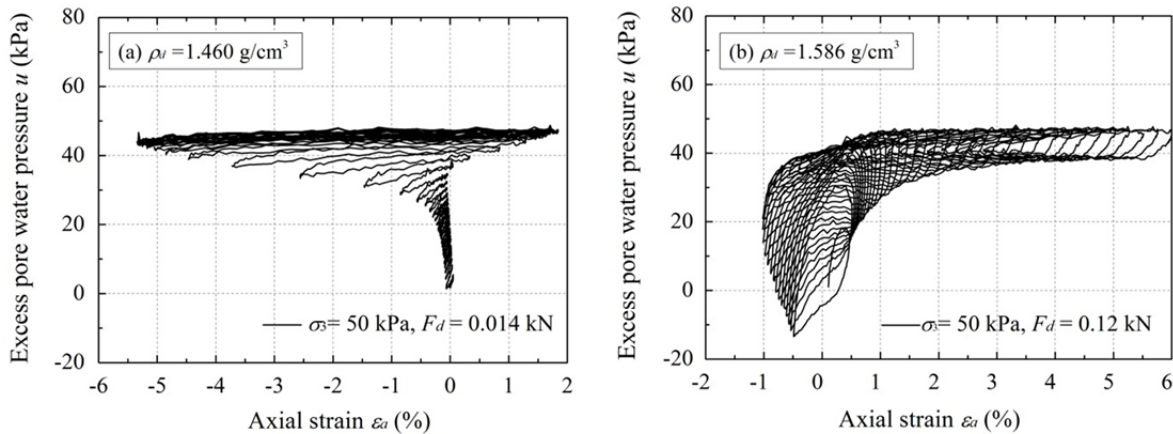

Figure 12 Relationship of the typical EPWP u versus the dynamic axial strain ε_a due to cyclic loading at a confining pressure of σ_3=50 kPa.
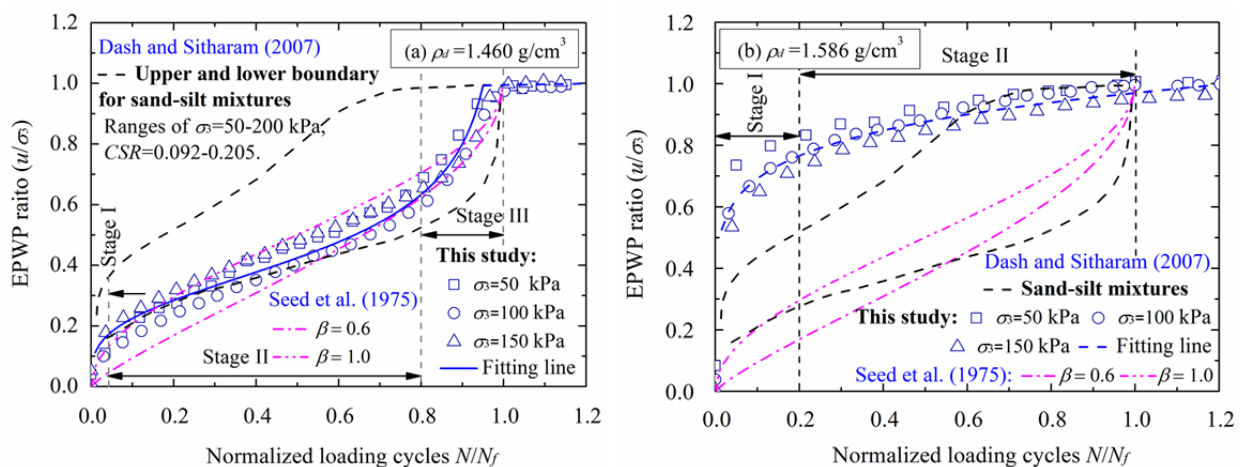

Figure 13 Excess pore water pressure (EPWP) ratio u/σ_3 versus normalized loading cycles N/N_f. (a) ρ_d=1.460 g/cm³; (b) ρ_d=1.586 g/cm³.

pressure. The u/σ_3 development is independent of the confining pressure. Different dry densities of saturated silt have different development characteristics for the EPWP ratio. Booker et al. (1976) proposed an alternative, somewhat simplified version of this equation:

$$u / \sigma_3 = \frac{2}{\pi} \cdot \arcsin(\frac{N}{N_f})^{1/2\beta} \qquad (11)$$

A value of β equal to 0.7 is traditionally assumed, as recommended by Seed et al. (1975), for clean sands. Recently, other authors have attempted to analyse the accuracy of the predictions from Seed's model with regard to silty sands (Polito et al. 2008; Baziar et al. 2011), but those aspects have not been fully quantified to date. Also plotted in Figure 13 are the upper and lower bound curves suggested by Seed et al. (1975) for clean sands corresponding to β values of 0.6 and 1.0, respectively. Moreover, as suggested by Dash & Sitharam (2009) and Karim & Alam (2014), the upper and lower bounds of the peak pore pressures generated in sand-silt mixture specimens over a wide range of parameters have also been presented as a function of N/N_f in Figure 13 to compare the behavioural differences in silt samples.

The EPWP growth for the $\rho_d=1.460$ g/cm3 silt in the process of cyclic loading can be divided into three stages: I, fast growth, II, gentle development, and III, rapid increase. The critical loading cycles N/N_f for the stage divisions are 0.05 and 0.8. The EPWP dissipates in both loose silt and fine sand due to the magnitudes of their equivalent coefficients of permeability. In the early stage of cyclic loading ($N/N_f<0.05$, stage I), the EPWP transitions from fast growth to gradual growth, whereas in the later stage ($N/N_f >0.8$, stage III), the failure of the cohesional and frictional strengths among the particles leads to structure collapse and a rapid increase in the EPWP. The development mode of the EPWP in the loose silt is similar to that of fine sand, which is in accordance with a "fast-gentle-sharp" growth mode:

$$u / \sigma_3 = (\frac{a}{N / N_f} + b)^c \qquad (12)$$

where a, b, and c are the testing parameters. When $\rho_d=1.460$ g/cm3, $a=19.36$, $b=-19.34$, and $c=-0.29$.

The high-density silt ($\rho_d=1.586$ g/cm3) has a lower permeability coefficient than that of the fine

sand. In the initial stage of cyclic loading (N/N_f <0.2, stage I), the EPWP is not easily dissipated, u/σ_3 sharply increases to 0.77, and the pore structure is partially destroyed. The rate of increase of u/σ_3 decreases in the later stage of cyclic loading ($N/N_f >0.2$, stage II) and gradually stabilizes at a value of 1. Due to the presence of clay particles ($P_c=6.3\%$), some residual cohesion and structural strength remains in the silt (Table 2). New drainage channels gradually form in the pores, resulting in a steady rise in the EPWP, which approaches the confining pressure. The growth characteristics of the EPWP of dense silt are significantly different from those of fine sand (Yamamuro et al. 2008; Izadi et al. 2008) and loose silt. The EPWP "fast-stable" growth mode follows the power function model:

$$u / \sigma_3 = b(N / N_f)^a \qquad (13)$$

where a, b, and c are the testing parameters. When $\rho_d=1.586$ g/cm3, $a=0.147$, and $b=0.97$.

It can be observed that, only for the loose silt ($\rho_d=1.460$ g/cm3) (Figure 13a), most of the experimental data in this study fall inside the bounds suggested for clean sands by the Seed model. Conversely, for the dense silt ($\rho_d=1.586$ g/cm3) (Figure 13b), all experimental data fall outside of the suggested upper and lower bound curves suggested by the Seed model. Similarly, the experimental data of loose silt fall within the upper and lower boundary curves suggested for the sand-silt mixture by Dash & Sitharam (2009); however, some of the experimental data for the dense silt fall inside the boundary only when $N/N_f >0.6$. The formulation of the EPWP ratio proposed by Dash & Sitharam (2009) and Seed et al. (1975) was found to be valid for the loose silt used in this study. However, the abovementioned models are not suitable for the dense silt. A power function model obtained in this paper for the dense silt can well describe the EPWP growth characteristics.

2.2.5 Dynamic shear modulus and damping ratio

Figure 14 shows the typical axial stress-axial strain hysteresis loops of silt samples under a confining pressure of $\sigma_3=100$ kPa. Based on the dynamic stress-strain hysteresis loops, the dynamic shear modulus G_d and the damping ratio λ are obtained via Eq. (14) and Eq. (15), respectively.

$$G_d=\Delta\sigma/\Delta\varepsilon=(\sigma_{d,max}-\sigma_{d,min})/(\varepsilon_{N,max}-\varepsilon_{N,min}) \quad (14)$$

$$\lambda=A_L/\pi A_t \quad (15)$$

where $\sigma_{d,max}$ and $\varepsilon_{N,max}$ are the maximum values of the stress and strain at the highest points of one hysteresis loop, respectively; $\sigma_{d,min}$ and $\varepsilon_{N,min}$ are the minimum values of the stress and strain at the lowest points of the hysteresis loop, respectively; $\Delta\sigma$ is the stress increment; $\Delta\varepsilon$ is the strain increment; A_L is the area of the hysteresis loop, and A_t is A_t is the area of the triangle ΔABC.

As shown in Figure 14, the stress-strain hysteresis loops gradually fall to the strain axis, and the falling trends of the loops increase with an increase in the axial strain until liquefaction occurs. The width of the hysteresis loop is increasingly larger, that is, the damping in the soil is becoming increasingly larger. The greater the cyclic strain, the faster the axial stress decreases. Liquefaction of soil generally produces a large strain (>0.01%). The dynamic shear modulus G_d and the damping ratio λ_d are functions of the shear strain γ_d, namely, $G_d=G_d(\gamma_d)$, and $\lambda_d=\lambda_d(\gamma_d)$.

$$\gamma_d=(1+v)\varepsilon_a \quad (16)$$

where v is the Poisson ratio.

The dynamic shear modulus G_d and damping ratio λ_d are the major parameters used in soil dynamic response analysis. Figure 15 shows the variation in G_d with γ_d for the silt at $\sigma_3=100$ kPa. The silt sample density determines the initial value of G_d. The value of G_d of the dense silt is greater than that of the loose silt. The dynamic shear modulus G_d of the silt decreases with an increase in the γ_d. When $\gamma_d<0.01\%$, G_d decreases slowly with increasing γ_d. When $\gamma_d=0.01\%-1.0\%$ (range I), G_d quickly decreases with increasing γ_d. When $\gamma_d>1.0\%$ (range II), G_d decreases slowly and approaches 0 with increasing γ_d. Additionally, when $\gamma_d>1.0\%$, the differences in G_d between the dense silt and the loose silt become increasingly smaller with increasing γ_d.

Figure 16 shows the variation in the damping ratio λ_d of the silt with γ_d at $\sigma_3=100$ kPa. Under the same dynamic shear strain, the λ_d of the dense silt is always less than that of the loose silt. With an increase in γ_d, the value of λ_d of the saturated silt increases considerably. Similar to the $G_d-\gamma_d$ relationship, as γ_d increases within the small strain range (<0.01%), λ_d slowly increases from 0. λ_d increases rapidly as γ_d increases from 0.01% to 1.0%
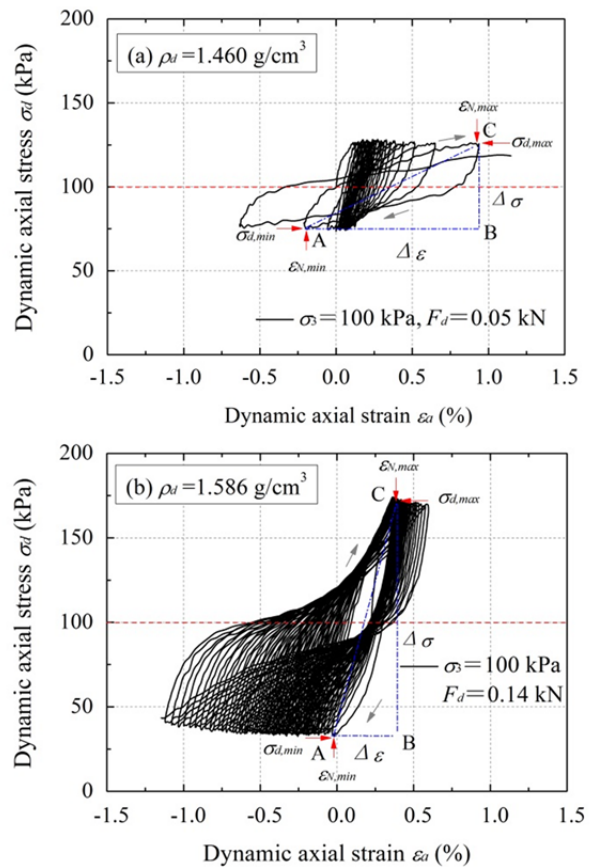

Figure 14 Stress-strain hysteresis loops of the silt sample at a confining pressure of $\sigma_3=100$ kPa: (a) $\rho_d=1.460$ g/cm³ and axial dynamic loads $F_d=0.05$ kN; (b) $\rho_d=1.586$ g/cm³ and $F_d=0.14$ kN.
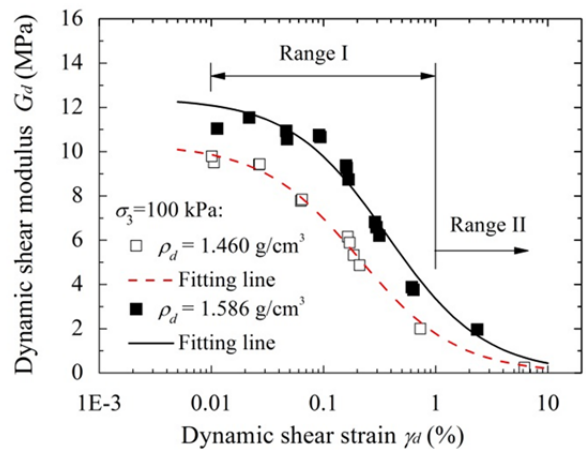

Figure 15 Relationship between the dynamic shear modulus G_d and dynamic shear strain γ_d of the silt at confining pressure $\sigma_3=100$ kPa.

(range I). When $\gamma_d>1.0\%$ (range II), λ_d increases gradually and approaches a constant value as γ_d increases. Under the small strains of $\gamma_d<0.01\%$, the silt is in the elastic deformation stage; therefore,
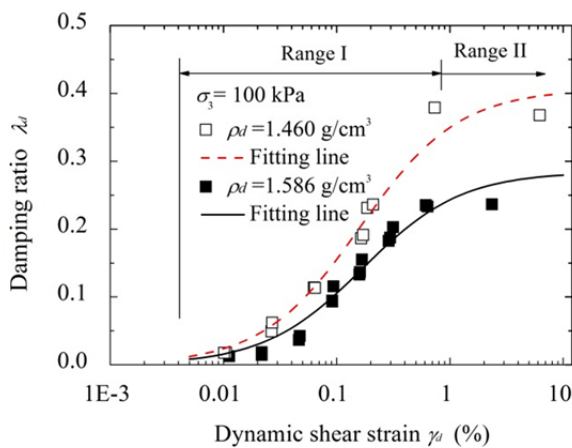
Figure 16 Relationship between the damping ratio λ_d and dynamic shear strain γ_d of the silt at confining pressure σ_3=100 kPa.

the initial G_d is approximately stable. Energy is not consumed in the elastic stage, and thus, the damping ratio λ_d is approximately 0. When γ_d=0.01%-1.0%, the silt soil reaches the elastic-plastic deformation states. With an increase in the shear strain γ_d, the silt granular dislocation causes plastic deformation, structural damage gradually increases, and G_d rapidly decreases. Plastic deformation leads to an increase in energy consumption and a rapidly increase in the damping ratio λ_d. When γ_d>1.0%, the structural collapse of the silt leads to uncontrollable shearing deformation; G_d decreases and approaches 0, and γ_d approaches a constant value.

Compared with the loose silt, the density of the silt increases, the particles of soil become more compact, and the stiffness increases, which causes the G_d to increase. With an increase in the dynamic shear modulus, the stress-strain hysteresis loop of the dense silt spreads more easily, that is, the damping ratio decreases eventually. Under small strains of γ_d <0.01%, both the dense silt and the loose silt are in the elastic deformation stage, and therefore, their initial dynamic shear modulus G_d is approximately unchanged. The dry density determines the initial dynamic shear modulus, and the higher density of the dense silt leads to a larger initial dynamic shear modulus. In the elastic-plastic deformation stage of silt, compared with the loose silt, the small strain of the dense silt under an earthquake is more advantageous for controlling the deformation of the silt slope or foundation. Under seismic activity, the damping ratio of dense

silt decreases, and the seismic shear stress is more easily transmitted in the dense silt, which results in greater dynamic shear stress. If a horizontal reinforcement (e.g., an anti-slide pile) is set in the slope body, it can not only reduce the lateral deformation of the slope but also share the horizontal shear stress. This method can greatly reduce the seismic shear stress in the slope, and it can bolster the anti-seismic effect of the horizontal reinforcement.

3 Conclusions

Under different cyclic shear stress ratios, 40 cyclic triaxial liquefaction tests were conducted on loose silt (ρ_d=1.460 g/cm^3) and dense silt (ρ_d=1.586 g/cm^3) to obtain the liquefaction assessment criteria, determine the liquefaction resistance, illustrate the dynamic strength, improve the growth model of the EPWP and clarify the relationship between the shear modulus and damping ratio.

(1) For the loose saturated silt, considering the influence of the response lag of the EPWP, a double-amplitude axial strain of 5% could accurately reflect the initial liquefaction assessment criteria. However, for the dense silt with a low permeability, an EPWP ratio of 1 is a more suitable liquefaction criterion.

(2) The cyclic stress ratio (*CSR*) of the loose silt increases with increasing confining pressure, whereas the *CSR* of the dense silt decreases with increasing confining pressure. The increase in the anti-liquefaction ability for the dense silt is more significant under a lower confining pressure.

(3) The *CSR* of loose silt falls well with the results of the sandy silt and Fraser River silt, which may be due to the similar dry densities. The influencing factors of the particle size, the physicochemical action of clay particles and the bonding effect of water in pores cause the dense silt to have a higher structural strength than the sand-silt mixtures and to more often exhibit higher liquefaction resistance than the sand-silt mixtures.

(4) The EPWP development of the loose silt is similar to that of the fine sands, following a "fast-gentle-sharp" growth pattern, and their critical loading cycles N/N_f are 0.05 and 0.80, respectively. However, the initial EPWP ratio of dense silt

increases quickly to 0.77 and increases slowly in the later stage ($N/N_f > 0.2$), gradually increasing the EPWP ratio to reach a value of 1.0.

(5) The formulation of the EPWP ratio proposed by Dash & Sitharam (2009) and Seed et al. (1975) was found to be valid for the loose silt used in this study. However, the above mentioned models are not suitable for the dense silt. The power function model can effectively describe the EPWP growth characteristics of the dense silt.

(6) Under seismic activity, the damping ratio of dense silt decreases, and the seismic shear stress is more easily transmitted in the dense silt, which results in greater dynamic shear stress. The horizontal reinforcement (anti-slide pile) can greatly reduce the seismic shear stress in the slope, and it can bolster the anti-seismic effect of the horizontal reinforcement.

Acknowledgements

References

Adhikari K, Subedi M, Sharma K, et al. (2018) Liquefaction Phenomenon in the Kathmandu Valley during the 2015 Earthquake of Nepal. World Academy of Science, Engineering and Technology. International Journal of Geological and Environmental Engineering 5(6).
http://doi.org/10.1999/1307-6892/81120

Alibolandi M, Ziaie Moayed R (2015) Liquefaction potential of reinforced silty sands. International Journal of Civil Engineering 13(3):195-202.
http://doi.org/10.22068/IJCE.13.3.195

ASTM, D.2487-98. (2011) Standard Practice for Classification of Soils for Engineering Purposes (Unified Soil Classification System). American Society for Testing and Materials, Philadelphia. pp 238-247.

Baziar MH, Sharafi H (2011) Assessment of silty sand liquefaction potential using hollow torsional tests-An energy approach. Soil Dynamics and Earthquake Engineering 31(7):857-865.
http://doi.org/10.1016/j.soildyn.2010.12.014

Baziar MH, Shahnazari H, Sharafi H (2011) A laboratory study on the pore pressure generation model for Firouzkooh silty sands using hollow torsional test. International Journal of Civil Engineering 9(2):126–34.
http://ijce.iust.ac.ir/article-1-489-en.html

Belkhatir M, Arab A, Schanz T, et al. (2011) Laboratory study on the liquefaction resistance of sand-silt mixtures: effect of grading characteristics. Granular Matter 13(5): 599-609.
http://doi.org/10.1007/s10035-011-0269-0

Beyzaei CZ, Bray JD, van Ballegooy S, et al. (2018) Depositional environment effects on observed liquefaction performance in silt swamps during the Canterbury earthquake sequence. Soil Dynamics and Earthquake Engineering 107: 303-321.
https://doi.org/10.1016/j.soildyn.2018.01.035

Booker JR, Rahman MS, Seed HB (1976) GADFLEA: a computer program for the analysis of pore pressure generation and dissipation during cyclic or earthquake loading (No. PB-263947; EERC-76-24). California Univ., Berkeley (USA). Earthquake Engineering Research Center.

Boulanger RW, Idriss IM (2004) Evaluating the potential for liquefaction or cyclic failure of silts and clays (p 131). Davis, California: Center for Geotechnical Modeling.

Chen GX, Jin DD, Chang XD, et al. (2013) Review of soil liquefaction characteristics during major earthquakes in recent twenty years and liquefaction susceptibility criteria for soils. Rock and Soil Mechanics 34(10): 2737-2755.
http://doi.org/10.16285/j.rsm.2013.10.005

Chen XQ, Chen JG, Cui P, et al. (2018) Assessment of prospective hazards resulting from the 2017 earthquake at the world heritage site Jiuzhaigou Valley, Sichuan, China. Journal of Mountain Science 15(4).
https://doi. org/10.1007/s11629-017-4785-1

Chegenizadeh A, Keramatikerman M, Nikraz H (2018) Liquefaction resistance of fibre reinforced low-plasticity silt. Soil Dynamics and Earthquake Engineering 104: 372-377.
https://doi.org/10.1016/j.soildyn.2017.11.004

Chiaro G, Koseki J, Sato T (2012) Effects of initial static shear on liquefaction and large deformation properties of loose saturated toyoura sand in undrained cyclic torsional shear tests. Soils & Foundations 52(3): 498-510.
http://doi.org/10.1016/j.sandf.2012.05.008

Dashti H, Sadrnejad SA, Ganjian N (2017) Multi-directional modeling for prediction of fabric anisotropy in sand liquefaction. Computers and Geotechnics 92: 156-168.
https://doi.org/10.1016/j.compgeo.2017.08.002

Dash HK, Sitharam TG (2009) Undrained cyclic pore pressure response of sand–silt mixtures: effect of nonplastic fines and other parameters. Geotechnical and Geological Engineering 27(4): 501-517.
https://doi.org/10.1007/s10706-009-9252-5

El Takch A, Sadrekarimi A, El Naggar H (2016) Cyclic resistance and liquefaction behavior of silt and sandy silt soils. Soil Dynamics and Earthquake Engineering 83: 98-109.
https://doi.org/10.1016/j.soildyn.2016.01.004

Gallagher PM, Mitchell JK (2002) Influence of colloidal silica grout on liquefaction potential and cyclic undrained behavior of loose sand. Soil Dynamics and Earthquake Engineering 22(9-12): 1017-1026.
http://doi.org/10.1016/S0267-7261(02)00126-4

GB50007-2002 (2002) Code for design of building foundation. Beijing China Architecture & Building Press. (In Chinese)

GB50487-2008 (2008) Code for water resources and hydropower engineering geological investigation. Beijing: Chinese Planning Press. (In Chinese)

GB50021-2001 (2009) Code for Investigation of Geotechnical Engineering. China Architecture & Building Press. (In Chinese)

GB50111-2006 (2009) Code for seismic design of railway engineering. Beijing: China Planning Press. pp 44-45. (In Chinese)

Georgiannou VN (2006) The undrained response of sands with additions of particles of various shapes and sizes. Géotechnique 56(9): 639-649. http://doi.org/10.1680/geot.2006.56.9.639

Guo H, Jiang WL, Xie XS (2011) Late-Quaternary strong earthquakes on the seismogenic fault of the 1976 M s 7.8 Tangshan earthquake, Hebei, as revealed by drilling and trenching. Science China Earth Sciences 54(11): 1696. http://doi.org/10.1007/s11430-011-4218-x

Guo XJ, Cui P, Li Y, et al. (2016) The formation and development of debris flows in large watersheds after the 2008 Wenchuan Earthquake. Landslides 13(1): 25-37. https://doi.org/10.1007/s10346-014-0541-6

Hsu YH, Ge L, Chiang MH (2017) Effects of Cyclic Triaxial Loading Rates on Liquefaction Behavior of Fine-Grained Soils. Geotechnical Hazards from Large Earthquakes and Heavy Rainfalls. Springer, Tokyo. pp 155-161. https://doi.org/10.1007/978-4-431-56205-4_14

Huang Y, Bao Y, Zhang M, et al. (2015) Analysis of the mechanism of seabed liquefaction induced by waves and related seabed protection. Natural Hazards 79(2): 1399-1408. https://doi.org/10.1007/s11069-015-1897-1

Hyde AF, Higuchi T, Yasuhara K (2006) Liquefaction, cyclic mobility, and failure of silt. Journal of geotechnical and geoenvironmental engineering 132(6): 716-735. http://doi.org/10.1061/(ASCE)1090-0241(2006)132:6(716)

Idriss IM, Boulanger RW (2008) Soil liquefaction during earthquakes. Earthquake Engineering Research Institute.

Izadi AM, Luna R, Stephenson RW (2008) Liquefaction behavior of Mississippi river silts. In Geotechnical Earthquake Engineering and Soil Dynamics IV, ASCE. pp 1-10. http://doi.org/10.1061/40975(318)93

Karim ME, Alam MJ (2014) Effect of non-plastic silt content on the liquefaction behavior of sand–silt mixture. Soil Dynamics and Earthquake Engineering 65: 142-150. https://doi.org/10.1016/j.soildyn.2014.06.010

Khan SA, Saeed Z, Khan A, et al. (2017) Assessment of soil liquefaction potential in defence housing authority, Karachi, Pakistan. International Journal of Economic Environment Geology 8(2): 63-68. http://www.econ-environ-geol.org/pdf/aug2017/8.pdf

Li ZY, Yuan XM (2016) Seismic damage summarization of site effect and soil liquefaction in 2016 Kaohsiung earthquake. Earthquake Engineering and Engineering Dynamics 36(3): 1-7. (In Chinese) http://doi.org/10.13197/j.eeev.2016.03.1.lizy.001

Meng QK, Miao F, Zhen J, et al. (2016) Impact of earthquake-induced landslide on the habitat suitability of giant panda in Wolong, China. Journal of Mountain Science 13(10): 1789-1805. https://doi.org/10.1007/s11629-015-3734-0

Monkul MM, Yamamuro JA (2011) Influence of silt size and content on liquefaction behavior of sands. Canadian Geotechnical Journal 48(6): 931-942. http://doi.org/10.1139/t11-001

Monkul MM, Etminan E, Şenol A (2016) Influence of coefficient of uniformity and base sand gradation on static liquefaction of loose sands with silt. Soil Dynamics and Earthquake Engineering 89: 185-197. https://doi.org/10.1016/j.soildyn.2016.08.001

Mahmoudi Y, Taiba AC, Belkhatir M, et al. (2016) Experimental investigation on undrained shear behavior of overconsolidated sand-silt mixtures: effect of sample reconstitution. Geotechnical Testing Journal 39(3): 515-523. https://doi.org/10.1520/GTJ20140183.

Okamura M, Noguchi K (2009) Liquefaction resistances of unsaturated non-plastic silt. Soils and Foundations 49(2): 221-229. https://doi.org/10.3208/sandf.49.221

Okamura M, Soga Y (2011) Effects of pore fluid compressibility on liquefaction resistance of partially saturated sand. Soil & Foundation 46(5): 695-700. https://doi.org/10.3208/sandf.46.695

Olson SM, Stark TD (2003) Yield strength ratio and liquefaction analysis of slopes and embankments. Journal of Geotechnical and Geoenvironmental Engineering 129(8): 727-737. https://doi.org/10.1061/(ASCE)1090-0241(2003)129:8(727)

Polito CP, Green RA, Dillon E, et al. (2013) Effect of load shape on relationship between dissipated energy and residual excess pore pressure generation in cyclic triaxial tests. Canadian Geotechnical Journal 50(11):1118-1128. https://doi.org/10.1139/cgj-2012-0379.

Polito CP, Green RA, Lee J (2008) Pore pressure generation models for sands and silty soils subjected to cyclic loading. Journal of Geotechnical and Geoenvironmental Engineering 134(10): 1490-1500. https://doi.org/10.1061/(ASCE)1090-0241(2008)134:10(1490)

Porcino DD, Diano V (2017) The influence of non-plastic fines on pore water pressure generation and undrained shear strength of sand-silt mixtures. Soil Dynamics and Earthquake Engineering 101: 311-321. https://doi.org/10.1016/j.soildyn.2017.07.015

Price AB, DeJong JT, Boulanger RW, et al. (2016) Effect of Prior Strain History on the Cyclic Strength and CPT Penetration Resistance of Silica Silt. In Geotechnical and Structural Engineering Congress 2016. pp 1664-1674. https://doi.org/10.1061/9780784479742.142

Qing H, Yi L, Yi Z, et al. (2015) Experimental study of earthquake liquefaction of saturated silt in Wuhan area. Electronic Journal of Geotechnical Engineering 20: 10103-10112. http://www.ejge.com/2015/Ppr2015.0662ma.pdf

Rahman MM, Baki MAL, Lo SR (2014) Prediction of undrained monotonic and cyclic liquefaction behavior of sand with fines based on the equivalent granular state parameter. International Journal of Geomechanics 14(2): 254-266. http://doi.org/10.1061/(ASCE)GM.1943-5622.0000316

Sağlam S, Bakır BS (2014) Cyclic response of saturated silts. Soil Dynamics & Earthquake Engineering 61: 164-175. http://doi.org/10.1016/j.soildyn.2014.02.011

Seed HB, Martin PP, Lysmer J (1975) The generation and dissipation of pore-water pressures during soil liquefaction. Geotechnical report no. EERC 75-26. Berkeley, CA: Univ. of California.

Shariatmadari N, Karimpour-Fard M, Shargh A (2017) Evaluation of liquefaction potential in sand–tire crumb mixtures using the energy approach. International Journal of Civil Engineering 1-11. https://doi.org/10.1007/s40999-017-0202-y

SL237-1999 (1999) Specification of Soil Test. China Water Resources and Hydropower Press, Beijing. (In Chinese)

SL299-1999 (1999) Specification of Soil Test. China Water Resources Press, Beijing, China. (In Chinese)

Sivathayalan S, Ha D (2011) Effect of static shear stress on the cyclic resistance of sands in simple shear loading. Canadian Geotechnical Journal 48(10): 1471-1484. http://doi.org/10.1139/t11-056

Stamatopoulos CA, Lopez-Caballero F, Modaressi-Farahmand-Razavi A (2015) The effect of preloading on the liquefaction cyclic strength of mixtures of sand and silt. Soil Dynamics and Earthquake Engineering 78: 189-200. https://doi.org/10.1016/j.soildyn.2015.07.004

Taiba AC, Belkhatir M, Kadri A, et al. (2016) Insight into the effect of granulometric characteristics on the static liquefaction susceptibility of silty sand soils. Geotechnical and Geological Engineering 34(1): 367-382. https://doi.org/10.1007/s10706-015-9951-z

Thevanayagam S (1998) Effect of fines and confining stress on undrained shear strength of silty sands. Journal of Geotechnical and Geoenvironmental Engineering 124(6): 479-491. http://doi.org/10.1061/(ASCE)1090-0241(1998)124:6(479)

Thevanayagam S, Veluchamy V, Huang Q, et al. (2016) Non-plastic silty sand liquefaction, screening, and remediation. Soil Dynamics and Earthquake Engineering 91: 147-159. https://doi.org/10.1016/j.soildyn.2016.09.027

Tsaparli V, Kontoe S, Taborda DMG, et al. (2017) An energy-based interpretation of sand liquefaction due to vertical ground motion. Computers and Geotechnics 90: 1-13. https://doi.org/10.1016/j.compgeo.2017.05.006

Wang S, Luna R, Stephenson RW (2011) A slurry consolidation approach to reconstitute low-plasticity silt specimens for laboratory triaxial testing. Geotechnical Testing Journal 34(4): 288-296. http://doi.org/10.1520/GTJ103529

Wang S, Luna R, Yang J (2016) Reexamination of effect of plasticity on liquefaction resistance of low-plasticity fine-grained soils and its potential application. Acta Geotechnica 11(5): 1209-1216. https://doi.org/10.1007/s11440-015-0394-8

Wijewickreme D, Sanin MV, Greenaway GR (2005) Cyclic shear response of fine-grained mine tailings. Canadian Geotechnical Journal 42(5): 1408-1421. https://doi.org/10.1139/t05-058

Yamamuro JA, Lade PV (1997) Static liquefaction of very loose sands. Canadian Geotechnical Journal 34(6): 905-917. http://doi.org/10.1139/t97-057

Yamamuro JA, Covert KM (2001) Monotonic and cyclic liquefaction of very loose sands with high silt content. Journal of Geotechnical and Geoenvironmental Engineering 127(4): 314-324. http://doi.org/10.1061/(ASCE)1090-0241(2001)127:4(314)

Yamamuro JA, Wood FM, Lade PV (2008) Effect of depositional method on the microstructure of silty sand. Canadian Geotechnical Journal 45(11): 1538-1555. http://doi.org/10.1016/j.soildyn.2004.06.004